ADVANCED MATERIALS
www.advmat.de

Tunable 2D Electron- and 2D Hole States Observed at $Fe/SrTiO_3$ Interfaces

*Pia M. Düring, Paul Rosenberger, Lutz Baumgarten, Fatima Alarab, Frank Lechermann, Vladimir N. Strocov, and Martina Müller**

Oxide electronics provide the key concepts and materials for enhancing silicon-based semiconductor technologies with novel functionalities. However, a basic but key property of semiconductor devices still needs to be unveiled in its oxidic counterparts: the ability to set or even switch between two types of carriers—either negatively (n) charged electrons or positively (p) charged holes. Here, direct evidence for individually emerging n- or p-type 2D band dispersions in STO-based heterostructures is provided using resonant photoelectron spectroscopy. The key to tuning the carrier character is the oxidation state of an adjacent Fe-based interface layer: For Fe and FeO, hole bands emerge in the empty bandgap region of STO due to hybridization of Ti- and Fe- derived states across the interface, while for Fe_3O_4 overlayers, an 2D electron system is formed. Unexpected oxygen vacancy characteristics arise for the hole-type interfaces, which as of yet had been exclusively assigned to the emergence of 2DESs. In general, this finding opens up the possibility to straightforwardly switch the type of conductivity at STO interfaces by the oxidation state of a redox overlayer. This will extend the spectrum of phenomena in oxide electronics, including the realization of combined n/p-type all-oxide transistors or logic gates.

1. Introduction

Conductivity in electronic materials originates either from negatively (n) charged electrons or positively (p) charged holes. When n- or p-type carriers are confined at interfaces between semiconductors or insulators, either a two-dimensional electron system (2DES) or -hole system (2DHS) can form, providing the physical grounds for all transistor-type devices and quantum wells exploited in semiconductor (SC) technology. Metal-oxide SCs exhibit more versatile properties than silicon or metal-nitride SCs, such as the coexistence of ferromagnetism and superconductivity,[1] large spin splitting, and large magnetoresistance[2,3]—if it were not for the fact that there are many n-type but very few p-type metal-oxide materials.

The existence of a 2DES was first observed at the oxide-oxide interface of the now classic $LaAlO_3$ (LAO)/$SrTiO_3$ (STO)

P. M. Düring, P. Rosenberger, M. Müller
Fachbereich Physik
Universität Konstanz
78457 Konstanz, Germany
E-mail: martina.mueller@uni-konstanz.de

P. Rosenberger
Fakultät Physik
Technische Universität Dortmund
44221 Dortmund, Germany

L. Baumgarten
Forschungszentrum Jülich GmbH
Peter Grünberg Institut (PGI-6)
52425 Jülich, Germany

F. Alarab, V. N. Strocov
Paul Scherrer Institute
Swiss Light Source
Villingen PSI CH-5232, Switzerland

F. Lechermann
Institut für Theoretische Physik III
Ruhr-Universität Bochum
44780 Bochum, Germany

The ORCID identification number(s) for the author(s) of this article can be found under https://doi.org/10.1002/adma.202309217

DOI: 10.1002/adma.202309217

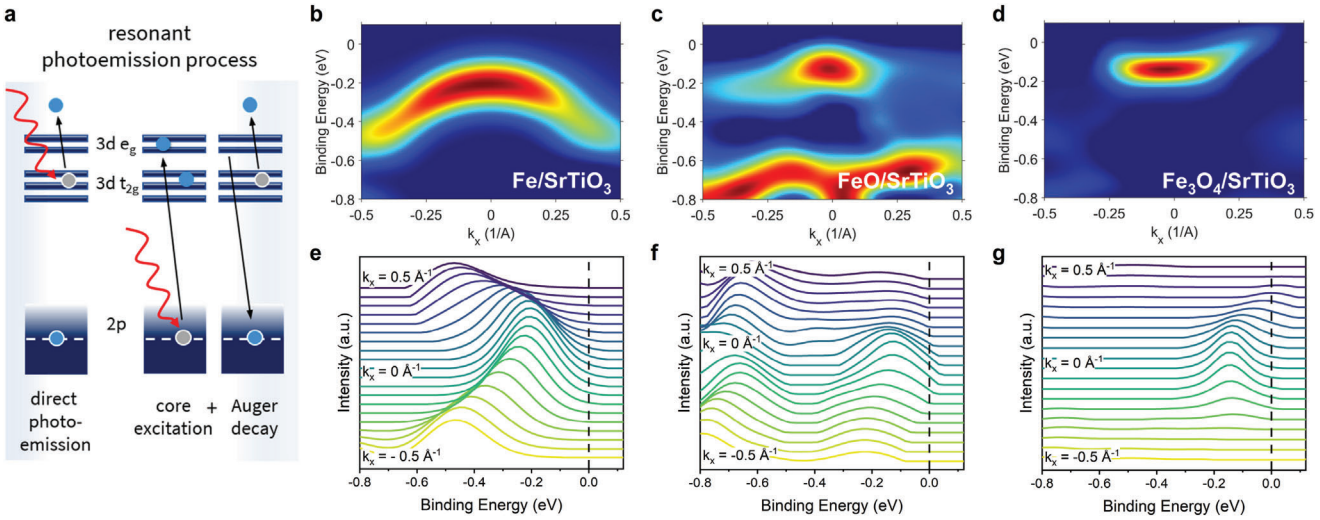

Figure 1. Energy dispersion maps of p- and n-type valence bands emerging in the otherwise empty band gap at Fe–$SrTiO_3$ interfaces. a) Schematics of the resonant soft x-ray photoemission process boosting the spectroscopic contrast for the Ti 3*d*-derived states at the buried Fe–$SrTiO_3$ interfaces. b–d) Energy dispersion maps $E(\mathbf{k})$ of the valence bands just below the Fermi level for b) Fe/STO, c) FeO/STO, and d) Fe_3O_4/STO interfaces. The photon excitation energy was set to the resonant Ti $L_{3/2}$ absorption edge at $h\nu = 466$ eV using circular- (c+) and s-polarized X-rays, thereby capturing d_{xz}, d_{yz}, and d_{xz} (c+ pol.) as well as d_{yz} and d_{xz} (s-pol.) bands, respectively. Depending on the particular Fe–$SrTiO_3$ interface, either hole- or electron band dispersions emerge in the otherwise unoccupied bandgap of STO. The intense resonant behavior of these gap states demonstrates their high degree of localization on the Ti atoms. The emergence of either hole- or electron band character depends on the specific interface chemistry of the Fe–$SrTiO_3$ heterostructures. e–g) Corresponding energy distribution curves (EDCs) after background correction, see Experimental Section.

heterostructure,[4] and to date at numerous other STO-based systems. More recently, a 2DHS was found in a STO/LAO/STO trilayer structure—but coexisting with a spatially separated 2DEG, making individual addressing of hole-related properties difficult.[5] Perfectly sharp and crystalline ordered interfaces were necessary to stabilize a 2DES and combined 2DHS/2DEG in the $LaAlO_3$ (LAO)/$SrTiO_3$ (STO)-based heterostructures,[4,5] and to suppress the formation of oxygen vacancies (V_O).

Individual 2D hole-type conductivity at metal oxide interfaces was recently revealed in amorphous and air-exposed AlO_x/Fe_xO_y/STO systems by electrical transport experiments, reporting high mobilities up to 24.000 $cm^2\ V^{-1}\ s^{-1}$.[6] A sign change in the Hall voltage was interpreted as a switching from mainly hole to mainly electron-type carrier conduction above a Fe_xO_y threshold thickness of 0.20 nm. The transition from p- to n-type conduction was associated with an increase of oxygen vacancies at the $SrTiO_3$ interface due to the scavenging of oxygen with increasing Fe metal coverage, while p-type carriers were assigned to Fe-related cation hole doping in the $SrTiO_3$.[7]

The respective physical origins of 2DES and 2DHS emerging at STO-based interfaces are still subject of intense debate. In the case of 2DES, models describe very different scenarios that are result of either polar catastrophe,[8] formation of oxygen vacancies, quantum confinement or cationic mixing at the interface. In particular, the reduction of Ti^{4+} to $Ti^{3+/2+}$ on the $SrTiO_3$ side of the interface and concomitant release of itinerant electrons is assumed to be the origin for the formation of 2DEGs when oxygen vacancies are formed. Experimentally, 2D band dispersions of free electrons have been observed at X-ray irradiated bare STO surfaces[9] and at redox-created STO interfaces, e.g., Al/STO[10] or Eu/STO.[11,12] However, direct evidence for the emergence of 2D hole character in terms of band dispersion at STO-based interfaces and knowledge of the corresponding $Ti^{3+/2+}$ interface chemistry remains elusive to date, why modeling is still pending.

Here, we demonstrate the emergence of individual, i.e., either hole- or electron-type band dispersions at Fe-based $SrTiO_3$ interfaces using angle-resolved photoelectron spectroscopy (ARPES) as a direct probe of the momentum-resolved occupied electronic band structure $E(\mathbf{k})$. The p- and n-type interfaces are generated by depositing ultrathin Fe (2 unit cells (uc)), FeO (2 uc), and Fe_3O_4 (1 uc) layers on TiO_2- terminated $SrTiO_3$ (100) substrates, see Experimental Section. We assign the corresponding $Ti^{3+/2+}$ interface chemistry determined by angle-integrated X-ray photoelectron spectroscopy (XPS) on as-grown, pristine and X-ray exposed Fe-based $SrTiO_3$ interfaces.

Soft x-ray excitation of photoelectrons increases the probing depth compared to conventional surface sensitive ultraviolet ARPES to several nanometers (nm), and thereby enables access to the electronic structure of buried interfaces.[13] A resonant enhancement of the Ti- and Fe-related valence band (VB) intensity is accomplished by scanning the photon energy across the Ti $L_{3/2}$ (466 eV) and Fe $L_{3/2}$ (710 eV) absorption edges, respectively. The resonant photoemission process is schematically depicted in **Figure 1a**. It causes an interference of the direct photoemission of a VB electron with the coincident two-step autoionization (Auger) process into the same final state, where, at the *L*-edges, the Auger contribution boosts the Ti/Fe signals.[13,14]

2. p- and n-Type $SrTiO_3$ Interfaces: Experiment and Theory

Figure 1b–d depicts the energy dispersion $E(\mathbf{k})$ of the valence bands right below the Fermi level E_F around the Γ point of the Brillouin zone (BZ). Whereas for bare STO substrates, no

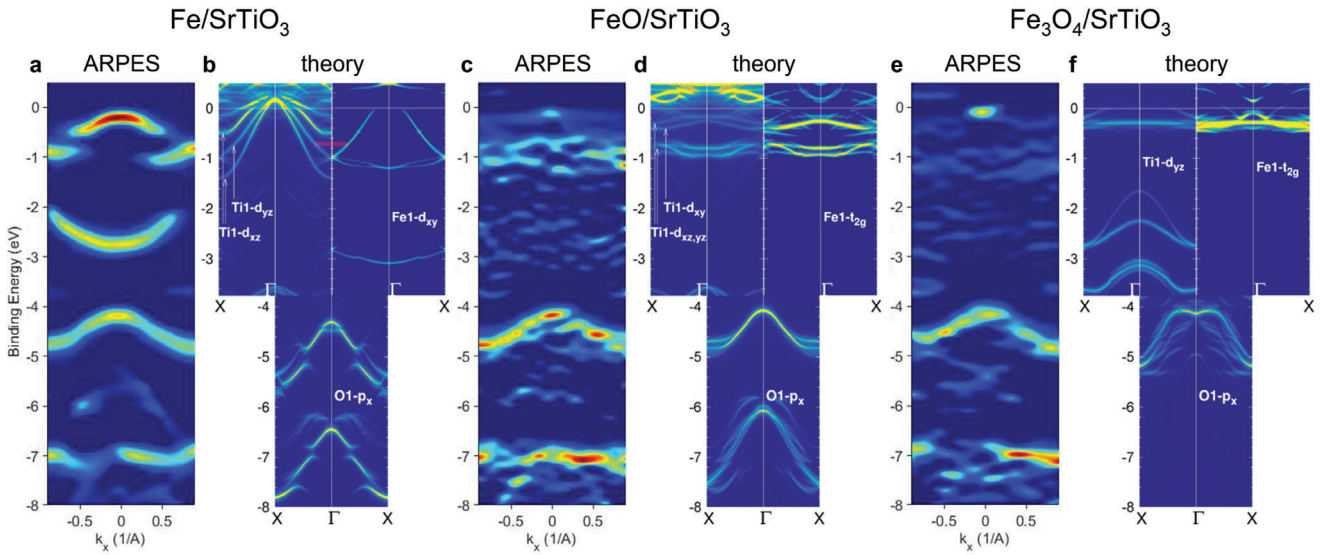

Figure 2. Experimental ARPES band structure and supercell calculations for Fe/STO, FeO/STO and Fe_3O_4/STO interfaces. a,c,e) Experimental band dispersions $E(\mathbf{k})$ along X–Γ –X for a) Fe/STO, c) FeO/STO and e) Fe_3O_4/STO interfaces, measured at the $Ti^{4+}t_{2g}$ resonance condition ($h\nu = 466$ eV) using c+ polarization. b,d,f) Corresponding first-principles dispersions obtained from projecting onto Ti, Fe, and O sites with *d* or *p* orbital character in the respective first ("1") interface layer. Ti1 (Fe1) projections are shown in the left (right) panels for the energy window [− 3.75, 0.5] eV and O1 projection in the bottom panels for the energy window [− 8, −3.75] eV. The red bar in (b) marks the low-energy hybridizing Ti1 d_{yz} and Fe1 d_{xy} branches. With increasing Fe oxidation state, the hole character of the dominant Ti1 $d_{xz,\,yz}$ dispersions systematically diminish their spectral weight.

states exist in the bandgap, the photoemission spectra of all Fe–$SrTiO_3$ interfaces show up dispersive Ti-related features, for which the spectroscopic contrast is resonantly enhanced. For the Fe/STO (b) and FeO/STO (c) interfaces, the valence bands bend parabolically downwards from a maximum centered at the zone centre Γ. This feature clearly indicates the existence of hole states with negative effective mass $\delta^2 E/\delta k^2 < 0$. At the Fe_3O_4/STO interface (d), in contrast, a dispersion with positive effective mass is observed at E_F, which is a hallmark for a 2D electron-like system.

The corresponding energy distribution curves (EDCs) are shown in Figure 1e–g. Details on the background correction are given in Experimental Section. We determine the hole band maxima at−200 meV (Fe/STO) and −110 meV (FeO/STO) below E_F, while the minimum of the confined electronic bands at the Fe_3O_4/STO interface is located at −120 meV. The lower binding energy of the p-band at the Fe/STO interface represents a higher hole energy compared to FeO/STO, but without cutting the Fermi level. For the FeO/STO sample, the hole band shifts upward to E_F. From the EDC in Figure 1f, we infer that the p-type hole band is closely approaching the Fermi level at the zone center Γ. Furthermore, the dispersive feature at the Fe_3O_4/STO interface crosses E_F at $k_x \approx \pm\, 0.3$ Å^{-1} and thus evidently represents a 2DES.

In order to capture the entire valence electronic structure of the Fe, Ti, and O subsystems, we show the extended ARPES images within the energy window from −8 to 0 eV in **Figure 2**a,c,e. The experimental energy dispersions $E(\mathbf{k})$ along X–Γ –X in the BZ are depicted for a) Fe/STO, c) FeO/STO, and e) Fe_3O_4/STO. In addition to the near-E_F region, as is shown in Figure 1b–d, here also the energetically lower Fe 3*d* and O 2*p* VBs become discernable. By using circularly (c+) polarized X-rays, the full manifold of the Ti 3*d* orbital-related band symmetries (d_{xz}, d_{yz}, and d_{xz}) was recorded.

A juxtaposition of the experimental ARPES results to first-principles supercell (SC) band structure calculations is given in Figure 2b,d,f. The theoretical dispersions were obtained from projecting onto the Ti, Fe, and O lattice sites and orbital characters (*d* and *p*) in the first layers adjacent to the interface (index "1"), see Figure S5 (Supporting Information). Here, we show the Ti1 (Fe1) projection on the left (right) panels for the energy window [− 3.75, 0.5] eV, and O1 projection (bottom panels) for the energy window [− 8, −3.75] eV. We note that the theoretical intensity of the Ti projections is multiplied by five to increase visibility, and low-intensity weight from projecting onto Fe states has been cut off. This procedure seems reasonable with regard to the experimental resonance condition enhancing the Ti contribution in the valence band. For the theoretical Fe_3O_4/STO case in Figure 2f, the single O1 projection misses the high-energy weight below −6 eV, because of inequivalent Fe/O sites of the inverse spinel lattice model. Extending the projection to additional O sites recovers that weight, but we have for brevity ignored this point.

The experimental dispersion features (Figure 2a,c,e) are in good accordance with the band structure calculations (Figure 2b,d,f) for the given Fe–$SrTiO_3$ interfaces. Especially the hole (p-type) character of the Fe/STO interface is well reproduced. Remarkably, above the STO O 2*p* VB, from ≈3.75 eV up to the Fermi level, the otherwise empty bandgap of $SrTiO_3$ is filled by a manifold of Ti 3*d*-derived states. Experimentally, in this energy range the Fe/STO interface is strongly dominated by a non-dispersive Fe 3*d* density of states, which is resonating at the Fe $L_{3/2}$ but not at the Ti $L_{3/2}$ edge (see Figure S3a,b, Supporting

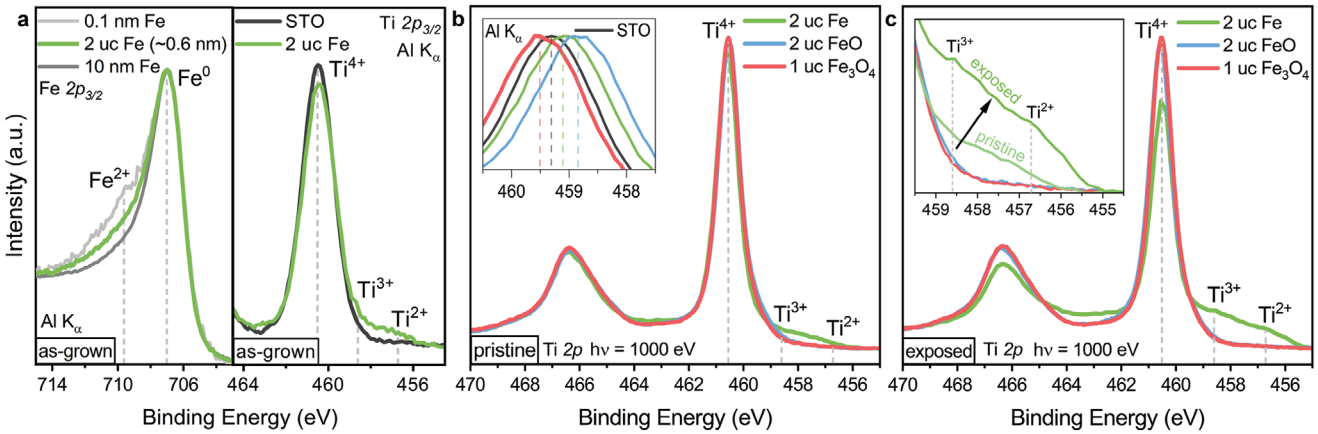

Figure 3. Interface chemical properties of Fe–$SrTiO_3$ samples in the as-grown, pristine and X-ray exposed states. a) XPS data of the as-grown Fe/$SrTiO_3$ sample recorded at RT. (left panel) Fe $2p_{3/2}$ core-level for three different Fe coverages indicating an interfacial Fe^{2+} compound. (right panel) Ti $2p_{3/2}$ core-levels of the $SrTiO_3$ substrate before and after Fe deposition, revealing a $Ti^{3+/2+}$ component after Fe deposition. b,c) Ti $2p_{3/2}$ and $2p_{1/2}$ core-levels of b) pristine and c) X-ray exposed Fe/STO, FeO/STO and Fe_3O_4/STO interfaces recorded at 12 K. No sizeable amount of $Ti^{3+,2+}$ is discerned for the FeO/$SrTiO_3$ and Fe_3O_4/$SrTiO_3$ samples in both states, while x-ray exposure further increases the $Ti^{3+,2+}$ weight at Fe/$SrTiO_3$ interface (inset c). All Ti $2p$ peaks are shifted and normalized for better comparison. Inset (b) shows the non-shifted, as measured energy positions of the Ti $2p_{3/2}$ peaks, from which the band alignment is estimated. XPS spectra of as-grown samples were collected using Al K_α radiation (1486.6 eV), while the pristine and exposed states were recorded at the synchrotron using $h\nu = 1000$ eV.

Information). The best agreement between SC calculations and experiment is achieved with regard to the leading Fe $3d$ orbital sectors with strongest spectral weight.

Additionally, the relevant Ti $3d$ low-energy spectral weight is generally smaller than the Fe $3d$ one, such that the effective Fe–Ti hybridization appears to be the main driving force behind the observed confined hole states. A further general key observation from theory is that only the directly adjacent TiO_2 and Fe(O) interface layers (here termed with index "1", respectively) need to be considered, since further layers more distant to the interface are not decisive for the hole vs electron characteristics. In particular on the relevant STO side, the hole state is confined solely within this first TiO_2 layer (or 1 uc), which is apparently different to, e.g., the more extended electron gas in LAO/STO. Among all Ti $3d$ states, the spectral weight of Ti $d_{xz,\,yz}$ orbitals dominates via energy-dependent hybridization to Fe t_{2g} over that of in-plane Ti d_{xy} states. For instance for the Fe/STO case in Figure 2b, the hole dispersion of Ti1-d_{yz} hybridizes with Fe1 d_{xy} (see red bar), and is thus well observable in the ARPES spectra. On the other hand, the Ti $3d$ weight on the deeper lying Fe1 d_{xy} dispersion between $[-3, -2]$ eV is much weaker. With regard to the hole character, we find the dominant Ti1 $d_{xz,\,yz}$ parabolic bands systematically diminishing their spectral weight with increasing Fe oxidation state (see energy window $[-0.75, 0]$ eV of left panels in Figure 2b,d,f). This theoretical trend is fully in line with the experimental results in Figure 2a,c,e. We note that E_F may be different for the real systems presumably including oxygen vacancies, see below.

3. Interface Chemical States and Driven Redox Processes

Obviously, the emergence of either hole- or electron band dispersions is closely linked to the specific chemical bonding at the Fe–$SrTiO_3$ interfaces. As we shall see in the following, it is reasonable to discriminate between growth- and X-ray-induced properties. To this end, XPS experiments were performed at three points in time; i) in the laboratory on the "as-grown" samples, ii) at the synchrotron using the intense x-ray beam on a fresh spot on the sample ("pristine") and iii) after >15 min illumination ("exposed"). Following the element-specific chemical binding energy (BE) shifts as well as the rigid BE shifts of all core-levels peaks allows to identify charge transfer, redox processes, and band bending at the Fe–$SrTiO_3$ interfaces, respectively.

Figure 3 compares the XPS spectra of p-type Fe/STO, FeO/STO and n-type Fe_3O_4/STO samples in their "as grown," "pristine," and "exposed" states. As becomes apparent from a visual inspection of the Ti $2p$ core-level line shapes, the p-type Fe/STO interface undergoes a redistribution of spectral weight—best observed on the lower binding energy side of the Ti $2p_{3/2}$ peak—first during growth (Figure 3a) and then during X-ray exposure (Figure 3b,c). In contrast, the n-type Fe_3O_4/STO and p-type FeO/STO samples remains almost unchanged. The reduction of Ti, which formally is associated with the transformation of Ti^{4+} to $Ti^{3+/2+}$ ions, results in a release of electrons. These excess negative charges are typically accompanied by the formation of single or even clustered oxygen vacancies V_O (in the case of Ti^{2+}) at the $SrTiO_3$ side of the interface, and screen these positively charged defects. Therefore, an intensity redistribution from the main Ti^{4+}-related peak to the $Ti^{3+/2+}$-related shoulder is commonly associated with the emergence of an n-type 2D electron system—but here is unexpectedly observed for the p-type Fe/STO interface. Vice versa, its almost absence in case of the n-type Fe_3O_4/STO sample is astonishing, too.

For creating the p-type Fe/STO interface, pure Fe metal was deposited onto TiO_2-terminated STO(001) surfaces (see Experimental Section). Fe has a much weaker oxygen affinity in comparison to other metals, e.g., Al[10] or Eu,[11,12] and therefore is significantly less prone to oxidation in contact with $SrTiO_3$. In

the present case, a small fraction of 10% Fe^{2+} spectral weight is discerned from the as-grown 2 uc Fe/STO spectra (see Figure 3a). The fractional oxidation from Fe^0 to Fe^{2+} can be associated with two different scenarios; it may arise from i) oxygen scavenging out of the $SrTiO_3$ substrate and redox-reaction to FeO or ii) diffusion of Fe into the STO topmost layer occupying Ti lattice sites.[7] A redox-reaction to FeO goes along with the formation of oxygen vacancies and the release of two excess electrons per V_O. This process is detectable from the "classical" Ti^{4+} to $Ti^{3+/2+}$ reduction signatures in Ti 2*p* photoemission spectra. On the other hand, a cation lattice site substitution Fe_{Ti} causes the transfer of both V_O electrons to the Fe_{Ti} site, making it Fe^{2+} valency.[7] In the last case, positively charged oxygen vacancies (holes) are created at the Fe/STO interface, but without a $Ti^{4+} \rightarrow Ti^{3+}$ reduction and without release of excess electrons. Instead, the thus formed $Fe_xTi_{1-x}O_{2-x}$ layer may cause an upward band shift of the STO (≈0.23 meV),[7] see below.

A well-known phenomenon in the field of X-ray photoelectron spectroscopy on $SrTiO_3$ is X-ray illumination creating a self-saturating amount of oxygen vacancies. Assorted experiments have demonstrated this effect for bare $SrTiO_3$ surfaces as well as for buried interfaces.[9,15,16] Light-induced V_O creation is also assigned to the formation of a 2D electron system at the $SrTiO_3$ interface, where the electron accumulation layer screens the V_O hole defects.[17] Comparing the Ti 2*p* core-level spectra in Figure 3 for b) pristine and c) exposed samples reveals the following evolution of the Fe–$SrTiO_3$ systems under X-ray illumination: For Fe/STO, we find a significant amount of $Ti^{3+,2+}$ emerging at the lower BE side of the Ti 2*p* doublet, which increased after X-ray exposure from ≈ 7 ± 2% ("pristine") to ≈18 ± 2% ("exposed"). In stark contrast, for the FeO/STO and Fe_3O_4/STO interfaces, the Ti 2*p* line shapes remain almost completely unaffected by X-ray illumination, hence no X-ray induced chemical process and oxygen vacancy formation are discernable from the Ti 2*p* core-level signatures. We note that the $SrTiO_3$ surfaces feature subtle experimental difference for subsequent Fe or FeO, Fe_3O_4 coverage: Before Fe deposition, the TiO_2-terminated $SrTiO_3$ surface is oxygen deficient due to annealing in vacuum, hence making it charge neutral.[18] Before FeO and Fe_3O_4 growth, in contrast, surface oxygen vacancies were annihilated by introducing molecular oxygen, see Experimental Section. Therefore, the recovered TiO_2-terminated $SrTiO_3$ surface is weakly polar.[18] To conclude on any light-induced oxygen release across the $SrTiO_3$ interface and possible reduction or oxidation reaction with the overlaying Fe, FeO, or Fe_3O_4 layers, we examined the Fe 2*p* core-levels in the pristine and exposed states (shown in the Supporting Information), but no changes of the line shapes could be discerned for Fe/$SrTiO_3$, FeO/$SrTiO_3$, and Fe_3O_4/$SrTiO_3$. Thus, the ARPES experiment unveils intrinsic hole-type interface states probably insensitive to X-ray illumination.

4. Band Alignment at Fe–$SrTiO_3$ Interfaces

Finally, the electrostatic interface properties need to be put into perspective. Both the presence of oxygen vacancies and concomitant screening by an electron accumulation layer as well as the polarity of adjacent intra-layers change the interfacial band alignment (BA) compared to the uncovered, undoped STO surface. To this end, the evolution of the interfacial BA is deduced as a flat band model from the rigid core-level BE shifts of the "as grown" sample set. For p-type Fe/STO and FeO/STO, the Ti 2*p* core-level spectra (see inset in Figure 3b) shift toward lower binding energy $\Delta E_{CL} = -0.48$ eV ($\Delta E_{CL} = -0.23$ eV), whereas a shifts to higher BE ($\Delta E_{CL} = 0.12$ eV) is observed in the case of Fe_3O_4/STO. From the XPS valence band spectrum of a bare STO substrate, we determine the O 2*p* valence band offset (VBO) at 3.05 ± 0.08 eV below the Fermi level. Assuming a bulk bandgap of 3.2 eV, this results in a conduction band offset (CBO) of 245 meV from E_F, see **Figure** 4b. We note that the actual STO bandgap likely depends on the V_O concentration.[19,20] A comparison of the interface formation scenarios as determined from the XPS analysis is sketched in Figure 4a. Qualitatively, the Fermi level shifts away from the CB toward the VB for Fe/STO and FeO/STO, whereas it moves toward or possibly into the CB at the Fe_3O_4/STO interface. The experimental parabolic p- and n-type dispersions as observed by ARPES are schematically included in Figure 4b.

5. Oxygen-Vacancy Independent Emergence of Hole- and Electron Dispersions

These experimental findings provide a differing and—according to current knowledge—unexpected scenario: A hole band dispersion is observed at the Fe/STO interface (see Figure 1b), but concurrently a growth-induced $Ti^{3+,2+}2p$ fraction that is moreover strongly increasing upon X-ray exposure (see Figure 3b,c). On the other hand, a 2DES emerges at the Fe_3O_4/STO interface (see Figure 1d), but without sizeable oxygen vacancy formation during growth or upon X-ray exposure as apparent from the typical Ti 2*p* core-level signatures (see Figure 3b,c). The FeO/STO case is caught right in-between; a hole-like dispersion is observed (Figure 1c), but oxygen vacancy formation upon growth and X-ray exposure is nearly absent (Figure 3b,c).

Our findings reveal that the emergence of either a hole- or electron dispersion at the Fe/STO interface in the present experiment is not critically affected by V_O formation—neither caused by oxygen scavenging during growth nor by X-ray illumination. The fact that the Fe/STO interface with such a clear signature of $Ti^{3+,2+}$ displays a hole-type dispersion is unprecedented, though.

From the band structure calculations, we infer that the hole-type valence band dispersion observed by ARPES for Fe/STO and FeO/STO interfaces originate from Fe 3*d* hybridization with Ti $3d_{xz,\,yz}$ states in the very first monolayer of the $SrTiO_3$ side of the interface. These interfacial hole states may be spatially well separated from a (probably coexisting but) subjacent electron accumulation, as suggested by the large oxygen vacancy concentration found for Fe/$SrTiO_3$.

The electron-type 2DES at the Fe_3O_4/STO interface likely originates from a downward-shift of the Ti 3*d* t_{2g} CBM and emerging itinerant electronic state at E_F. This dispersive quasiparticle state coexists with the in-gap state at −1.3 eV (see Figure S4c, Supporting Information), which is typically interpreted as a hallmark feature for the presence of oxygen vacancies in $SrTiO_3$.[15] The tiny if not absent $Ti^{3+,2+}2p$ core-level signature remains unanticipated, though.

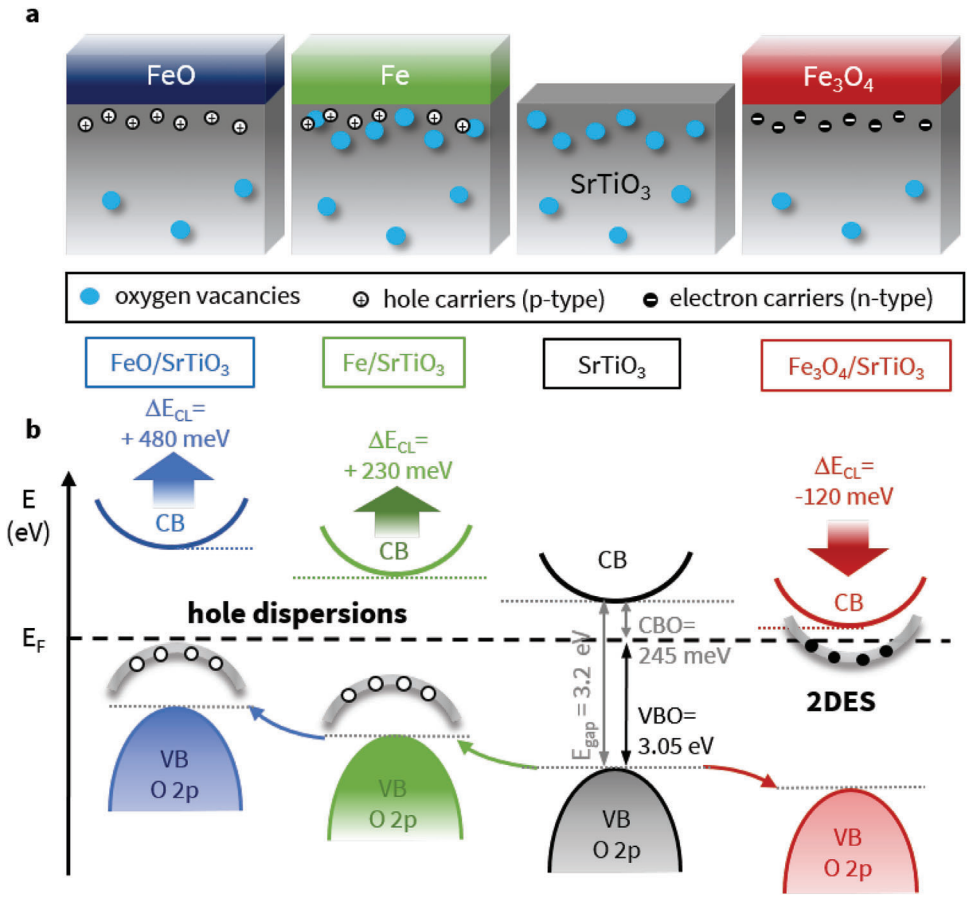

Figure 4. Experimentally derived interface formation and band alignment of Fe–$SrTiO_3$ heterostructures for different oxidation states of the Fe-based overlayers. a) Schematics of the Fe–$SrTiO_3$ interface formations as derived from XPS analysis. b) Schematic band alignment as determined from XPS. The valence band maximum of a bare $SrTiO_3$ substrate is located 3.05 eV below E_F (VB offset, VBO). Assuming an STO bandgap of $E_{gap} = 3.2$ eV, the unoccupied conduction band minimum is located 245 meV above the Fermi level (CB offset, CBO). From the rigid core-level shifts ΔE_{CL}, the respective band alignment was estimated for the of Fe/$SrTiO_3$ (+230 meV), FeO/$SrTiO_3$ (+480 meV) and Fe_3O_4/$SrTiO_3$ (−120 meV) interfaces. Whereas for Fe/$SrTiO_3$ oxygen vacancies are likely present at the interface, for FeO/$SrTiO_3$ and Fe_3O_4/$SrTiO_3$ no experimental hints in terms of $Ti^{3+/2+}$ contributions could be discerned.

6. Summary

To conclude, we provide direct evidence for individual hole- and electron-type valence band dispersions at Fe–$SrTiO_3$ heterostructures using momentum-resolved soft X-ray ARPES. Theoretical simulations suggest a model in which the respective band character is set by the Fe oxidation state of an Fe-based overlayer, which tunes hybridization between the Ti- and Fe-derived states across the interface. A p-type hole band emerges in the bandgap of insulating $SrTiO_3$ for ultrathin Fe or FeO coverages, respectively, while a 2D electron system is observed for Fe_3O_4 overlayers. The interface chemistry of the hole-type Fe/$SrTiO_3$ interface reveals a strong $Ti^{3+,2+}$ 2*p* contribution, which as of yet had been assigned exclusively to the emergence of 2DES and thus represents a novel case study in the field of 2D oxide interfaces. The results suggest the possibility to deliberately tune between n- or p-type conductivity at $SrTiO_3$-based oxide interfaces, and to exploit the Fe oxidation state to design the resulting band alignment. This experimental demonstration of individually emerging 2DHS and 2DES at $SrTiO_3$ interfaces may boost novel device concepts and developments, in particular realizing information processing devices with tunable n/p-conductivity—the so far missing link in oxide electronics.

7. Experimental Section

Sample Preparation: Samples were prepared on commercial TiO_2-terminated, undoped $SrTiO_3$ (001) substrates (from CrysTec) using molecular beam epitaxy (MBE) operated under ultrahigh vacuum (UHV) at a base pressure $p = 3 \times 10^{-11}$ mbar. The as-received, undoped $SrTiO_3$ (STO) substrates were annealed in UHV at 500°C for 30 min. This surface preparation process led to the reduction of the TiO_2 layers and formation of oxygen vacancies.[15,21]

Fe, FeO and Fe_3O_4 thin films with thicknesses of nominally 1 or 2 unit cells (uc) were prepared by e-beam evaporation of metallic Fe at a growth rate of 0.24 nm min^{-1} onto STO substrates kept at $T_S = 350$°C. For FeO and Fe_3O_4 preparation, molecular oxygen was stabilized before and constantly supplied during Fe evaporation at a pressure of $p_{O_2} = 3.3 \times 10^{-7}$ mbar. For Fe_3O_4, the oxygen supply was kept for additional 90 s after the Fe shutter was closed.

To prevent any (over-)oxidation of the Fe_xO_y/STO samples, a portable UHV suitcase (Ferrovac) with a base pressure in the 10^{-11} mbar range was

used to transport the samples in situ to the Swiss Light Source (SLS). All samples were transferred to the measurement chamber without breaking the UHV condition and, hence, without need for a capping layer.

In Situ Sample Characterization using LEED and XPS: The Fe-based overlayer thicknesses were determined during growth by an in situ quartz microbalance. To confirm the crystalline quality of substrates and as-grown films, low-energy electron diffraction (LEED) patterns were recorded in situ using a SPECS ErLEED-1000 on all samples at room temperature, respectively. For bare STO substrates, sharp reflections of the TiO_2-terminated surface were obtained, which blur out upon the deposition of 2 uc Fe, FeO, and 1uc Fe_3O_4, respectively, but without a geometrical change of the reflection pattern.

The chemical composition of the bare $SrTiO_3$ substrates and "as-grown" Fe/STO, FeO/STO, and Fe_3O_4/STO heterostructures was determined by in situ X-ray photoelectron spectroscopy (XPS) using non-monochromatized Al K_α radiation ($h\nu = 1486.6$ eV). A setup consisting of a SPECS XR-50 X-ray source and a SPECS Phoibos 100 analyzer was used.

Quantification of Fe_xO_y Film Thicknesses and Stoichiometry: In addition to the quartz microbalance reading during deposition, the Fe-based film thicknesses were cross-checked by XPS analysis of the Ti 2*p* core-level peak attenuation induced by the overlayer. Fe (≈0.63 nm)/STO, FeO (≈0.83 nm)/STO, and Fe_3O_4 (≈0.96 nm)/STO were determined, whereby the unit cell (uc) sizes for Fe, FeO, and Fe_3O_4 are 0.289, 0.43, and 0.839 nm, respectively.

The Fe film stoichiometry of the "as grown" samples was deduced from the relative positions of the spin-orbit split Fe $2p_{3/2}$ and $2p_{1/2}$ doublets, see Figure S1a (Supporting Information). For Fe^0 metal deposited on STO under UHV, they were located at ≈707 and ≈720 eV, respectively. For Fe deposited in an O_2 atmosphere onto $SrTiO_3$, we determine chemical shifts of the Fe 2*p* doublet toward higher binding energy (BE) indicating an oxidation to Fe^{2+} (FeO) and mixed Fe^{2+}/Fe^{3+} states (Fe_3O_4). For a quantitative analysis, a core-level line shape decomposition was performed using reference spectra of Fe metal (Fe^0), FeO (Fe^{2+}), and magnetite ($Fe^{2+,3+}$).[22,23] For FeO/STO the quantitative decomposition of the "as-grown" Fe 2*p* Lab-XPS spectra reveal a fraction of unoxidized, metallic Fe residuals of ≈10 ± 0.5%. For Fe_3O_4/STO, the "as-grown" Fe 2*p* Lab-XPS spectra revealed a fraction of divalent FeO residuals of ≈7 ± 0.5%.

The evolution of the Fe^{2+} peak shoulder was compared at ≈710 eV for "as-grown" Fe/STO samples with increasing Fe metal film thickness of 0.1, 0.6 (≈2 uc) and 10 nm, see Figure 3a. Clearly, the Fe^{2+} contribution was suppressed with respect to the Fe^0 main peak with increasing Fe metal coverage. This finding confirmed that the Fe^0 to Fe^{2+} oxidation took place directly at and originated from the STO interface. The estimated Fe^{2+}/Fe^0 ratio for the 2 u.c. Fe/STO sample was 10% and converted into an approximate thickness of ≈0.4 ML FeO.

Finally, it was confirmed that the line shapes of the Fe $2p_{3/2}$ and $2p_{1/2}$ core-levels for all three Fe–$SrTiO_3$ samples remained unchanged during X-ray exposure, although for Fe/STO, there was a change of the background visible in Figure S2 (Supporting Information).

Angle-Resolved Photoelectron Spectroscopy: ARPES measurements were performed at the soft x-ray ARPES endstation[24] of the Advanced Resonant Spectrocopies (ADRESS) beamline[14] of SLS, Paul Scherrer Institute, Switzerland. All experiments were performed with undoped STO substrates. A residual bulk conductivity necessary for PES experiments was facilitated by laser illumination of the samples, which had no measurable influence on the electronic structures. The samples were cooled to $T \approx 12$ K in order to quench the relaxation of k-conservation due to the thermal motion of the atoms.[25] The combined energy resolution (beamline plus analyzer PHOIBOS-150) was of the order of 40 meV for $E(\mathbf{k})$ maps, and the angular resolution of the analyzer was ≈0.1°. The photon flux was $\approx 10^{13}$ photons s^{-1} and focused onto a spot of 30 × 75 μm^2 on the sample surface. Variable polarization allowed symmetry analysis of the electron states. All reported ARPES data were collected after more than 1 h of irradiation time to ensure saturation of X-ray induced processes.

Resonant Photoelectron Spectroscopy Intensity Maps: A schematics of the resonant photoemission (resPE) process is sketched in Figure 1a. The Ti $L_{3/2}$ edge resonant photoemission intensity maps for a) 2 uc Fe/STO, b) 2 uc FeO/STO, and c) 1 uc Fe_3O_4/STO interfaces measured at $T = 12$ *K* and angle-integrated within $\pm k^{yz}$ are depicted in the Supporting Information Figure S3a–c (Supporting Information). The resonant photoemission intensity maps across the Fe $L_{3/2}$ absorption edges for d) 2 uc Fe/STO, e) 2 uc FeO/STO, and f) 1 uc Fe_3O_4/STO are shown in Figure S3d–f (Supporting Information).

Analyzing Figure S3 (Supporting Information), the spectral weight extending from −8 to −4 eV BE is the STO valence band (VB) formed by O(2*p*) states that hybridize with Ti(3*d*) and, expectable strongly resonate at the $Ti^{4+}t_{2g}$ and e_g absorption edge. Above the STO VB, from −3 eV BE up to the Fermi level, the otherwise empty band gap of $SrTiO_3$ is superimposed by metallic states. For a) Fe/STO, this energy range was strongly dominated by an incoherent and non-resonating Fe(3*d*) density of states, which were localized in the Fe overlayer. For c) Fe_3O_4/STO, resonating in-gap states emerge around −1.3 eV.

Differential spectra between the on- and off-resonant PES maps across the Ti $L_{3/2}$ absorption edges confirmed the accentuated increase of Ti spectral weight at the $Ti^{4+}t_{2g}$ peaks, see Figure S4 (Supporting Information), and were calculated from photon energies $h\nu = 466$ eV and $h\nu = 456$ eV, respectively. The spectral intensity at/below the Fermi level that was resonating with the Ti $L_{3/2}$ absorption edge was clearly extracted. In the case of pure STO, spectral intensity at −1.3 eV is usually related to oxygen vacancy-induced in-gap states resonating at the $Ti^{3+}e_g$ absorption peak,[26] which due to superposition is not discernable for Fe/STO and FeO/STO.

ARPES Data Analysis and resPES Image Processing: The raw data of the angular resolved resonant valence band structure were a superposition of a **k**-dispersive spectral fraction with a strong **k**-integrated background. For data analysis and graphical data processing, the **k**-integrated background contribution was simulated by angle integration of the PE intensity. Properly weighted, it was subtracted from the experimental spectra to uncover the **k**-dispersive fraction. These dispersive structures displayed in Figure 1b–d were extracted by taking the maximum curvature of the smoothed photoemission intensity along the BE direction.[27] This data analysis used MATLAB-based software ARPESView for viewing and processing of the ARPES data.[28]

Band Structure Calculations: Electronic band structures were calculated using a first-principles approach building up on a mixed-basis pseudopotential scheme based[29,30] on Kohn–Sham density functional theory (DFT) supplemented by an additional treatment of electronic correlations. Norm-conserving pseudopotentials and a mixed basis consisting of localized functions and plane waves were utilized. Localized functions were introduced for Ti(3*d*), Fe(3*p*, 3*d*), and O(2*s*, 2*p*). A plane-wave cutoff energy of $E_{cut} = 11$ Ry and a 7 × 7 × 1*k*-point mesh are used for the final supercell calculations.

To reveal the spectral data, the DFT+sic[31,32] methodology was utilized, which was suited to include electronic correlations beyond conventional DFT in an efficient way for large-scale supercell computation. It corresponded to overall applying the local density approximation (LDA) but employing here an oxygen pseudopotential that was modified by the self-interaction correction (SIC)[33] in order to address local Coulomb interactions. While the O(2*s*) orbital was by default fully corrected with a weight factor $w_{2s} = 1.0$, the reasonable choice[32,34] $w_{2p} = 0.8$ was utilized for the O(2*p*) orbitals. A further screening parameter α for this SIC pseudopotential was also chosen as $\alpha = 0.8$, such that the SIC inclusion on oxygen asks for one additional parameter in the overall computational scheme. Note that the description of electronic correlations originating here only from the oxygen sites may be a good approximation for weakly-to-moderately correlated systems, because of the hybridization between transition-metal and oxygen sites. For instance, such a plain DFT+sic approach to the moderately correlated metal $SrVO_3$ results in a low-energy band renormalization of $Z \approx 0.6$, in very good agreement with experiment. In the present context, application of this DFT+sic setting to bulk STO led to a bandgap $\Delta = 2.8$ eV close to the experimental value, while conventional DFT usually yields $\Delta \approx 2$ eV.

Tetragonal supercells in slab architecture based on a 1 × 1 in-plane motif were constructed for the three structural cases of Fe/STO (69 atoms), FeO/STO (85 atoms) and Fe_3O_4/STO (81 atoms) as shown in the

respective upper part of Figure S5 (Supporting Information). Symmetric slabs with in total 11 TiO_2 layers for the STO part are chosen. There were thus six layer-inequivalent Ti sites, with the mirror plane passing through the $Ti6O_2$ layer. On top of each STO surface, four Fe layers with and without oxygen coordination were added, whereby the first Fe1 layer was placed on top of the O1 positions of STO, respectively. This positioning was energetically favored compared to Fe on top of Ti. For Fe/STO case, a bcc-Fe coordination was realized, while FeO on STO amounted to a three-dimensionally alternating, i.e., simple-cubic Fe,O lattice. Concerning Fe_3O_4/STO, for computational reasons the bulk Fe_3O_4 structure with differentiation of octahedral and tetrahedral Fe sites was not employed. Instead a structural approximant, building up on iron vacancies in the FeO layers tailored to the Fe_3O_4 stoichiometry was chosen. Note that the true Fe_3O_4/STO structure might not be fully ordered in the Fe_3O_4-bulk sense, and therefore the approximant was believed to be a meaningful description to evaluate the key features of the Fe_3O_4/STO electronic structure. The experimental STO lattice parameter $a = 3.905$ Å was utilized for all structures and structural relaxation within the generalized-gradient approximation was performed to optimize the atomic positions, resulting in different layer-to-layer distances and local distortions. Note that the Ti5,Ti6 (and connected Sr,O sites) positions were kept fixed to the experimental STO lattice positions, in order install the "STO bulk limit" within the interior of the slabs. The relaxed vacuum region between periodically repeated slabs along the *c* direction amounts to a safe distance of 22–25 Å depending on the structural case. The nearest-neighbor (NN) Fe1-O1 distance reads $d_{Fe1\text{-}O1} = 1.942$ Å for Fe/STO, $d_{Fe1\text{-}O1} = 1.926$ Å for FeO/STO and $d_{Fe1\text{-}O1} = 1.935$ Å for Fe_3O_4/STO. The NN Fe1–Fe1 distance differs only slightly from the value $d_{Fe1\text{-}Fe1} = 2.76$ Å throughout the different structural cases.

The lower part of Figure S5 (Supporting Information) shows correspondingly the projected Fe(3*d*) and Ti 3*d* density of states (DOS). Nonsurprisingly, the Fe 3*d* DOS extended over a wide energy range into the original STO band gap. The largest extension for Fe/STO case was easily understood from the highly itinerant bcc-Fe overlayers. The more correlated FeO and Fe_3O_4 overlayers resulted in an effective Fe(3*d*) bandwidth reduction. The Ti(3*d*) low-energy states of exclusive $t_{2g} = \{xz, yz, xy\}$ kind were in all cases dissolved in the Fe 3*d* background. Notable Ti $e_g = \{z^2, x^2 - y^2\}$ weight, most prone to O 2*p* hybridization, resided at higher energies up and below the Fermi level. Oxygen vacancies were effective in bringing such e_g weight to lower energies (not shown). Note that the dominantly dispersing Ti $d_{xz,\,yz}$ character shown in Figure 2 was associated with the Ti1 sites, respectively. The notable Ti d_{xy} low-energy character, best visible in the outermost right part of Figure S5 (Supporting Information), was associated with contributions from the deeper Ti layers, mostly Ti2–Ti4.

Supporting Information

Supporting Information is available from the Wiley Online Library or from the author.

Acknowledgements

The authors thank T. Szyjka for help with the XPS analysis. F.L. acknowledges support from the European XFEL and the Center for Computational Quantum Physics of the Flatiron Institute under the Simons Award ID 825141. Computations were performed at the JUWELS Cluster of the Jülich Supercomputing Centre (JSC) under projects hhh08 and miqs. F.A. thanks the Swiss National Science Foundation for financial support within the grant 200020B-188709. M.M. acknowledges funding by the Deutsche Forschungsgemeinschaft (DFG, German Research Foundation), SFB 1432 (Project B03) with Project-ID 425217212.

Open access funding enabled and organized by Projekt DEAL.

Author Contributions

M.M. conceived the experiment. P.R. performed preliminary experiments. P.M.D. deposited and characterized the samples. P.M.D., P.R., M.M., F.A. and V.N.S. performed the ARPES experiments. P.M.D. performed the ARPES analysis under supervision of V.N.S. P.M.D. performed the XPS- and band alignment analysis under supervision of M.M. and L.B. P.M.D., L.B., V.N.S. and M.M. interpreted the experimental data with help of all co-authors. F.L. conceived the theory part and performed the simulations. M.M. and F.L. wrote the manuscript with help of all co-authors.

Conflict of Interest

The authors declare no conflict of interest.

Data Availability Statement

The data that support the findings of this study are available from the corresponding author upon reasonable request.

Keywords

2D electron gases, 2D hole gases, oxide interfaces, oxide-based electronics

Received: September 7, 2023
Revised: October 27, 2023
Published online: February 8, 2024

[1] N. Reyren, S. Thiel, A. D. Caviglia, L. F. Kourkoutis, G. Hammerl, C. Richter, C. W. Schneider, T. Kopp, A.-S. Rüetschi, D. Jaccard, M. Gabay, D. A. Muller, J.-M. Triscone, J. Mannhart, *Science* **2007**, *317*, 1196.
[2] A. Brinkman, M. Huijben, M. van Zalk, J. Huijben, U. Zeitler, J. C. Maan, W. G. van der Wiel, G. Rijnders, D. H. A. Blank, H. Hilgenkamp, *Nat. Mater.* **2007**, *6*, 493.
[3] J. S. Lee, Y. W. Xie, H. K. Sato, C. Bell, Y. Hikita, H. Y. Hwang, C. C. Kao, *Nat. Mater.* **2013**, *12*, 703.
[4] A. Ohtomo, H. Y. Hwang, *Nature* **2004**, *427*, 423.
[5] H. Lee, N. Campbell, J. Lee, T. J. Asel, T. R. Paudel, H. Zhou, J. W. Lee, B. Noesges, J. Seo, B. Park, L. J. Brillson, S. H. Oh, E. Y. Tsymbal, M. S. Rzchowski, C. B. Eom, *Nat. Mater.* **2018**, *17*, 231.
[6] L. D. Anh, S. Kaneta, M. Tokunaga, M. Seki, H. Tabata, M. Tanaka, S. Ohya, *Adv. Mater.* **2020**, *32*, 1906003.
[7] S. A. Chambers, Y. Du, M. Gu, T. C. Droubay, S. P. Hepplestone, P. V. Sushko, *Chem. Mater.* **2015**, *27*, 4093.
[8] N. Nakagawa, H. Y. Hwang, D. A. Muller, *Nat. Mater.* **2006**, *5*, 204.
[9] A. F. Santander-Syro, O. Copie, T. Kondo, F. Fortuna, S. Pailhès, R. Weht, X. G. Qiu, F. Bertran, A. Nicolaou, A. Taleb-Ibrahimi, P. Le Fèvre, G. Herranz, M. Bibes, N. Reyren, Y. Apertet, P. Lecoeur, A. Barthélémy, M. J. Rozenberg, *Nature* **2011**, *469*, 189.
[10] T. C. Rödel, F. Fortuna, S. Sengupta, E. Frantzeskakis, P. L. Fèvre, F. Bertran, B. Mercey, S. Matzen, G. Agnus, T. Maroutian, P. Lecoeur, A. F. Santander-Syro, *Adv. Mater.* **2016**, *28*, 1976.
[11] P. Lömker, T. C. Rödel, T. Gerber, F. Fortuna, E. Frantzeskakis, P. Le Fèvre, F. Bertran, M. Müller, A. F. Santander-Syro, *Phys. Rev. Mater.* **2017**, *1*, 062001.
[12] P. Lömker, M. Müller, *Phys. Rev. Mater.* **2019**, *3*, 061401.
[13] V. N. Strocov, C. Cancellieri, A. S. Mishchenko, *Spectroscopy of Complex Oxide Interfaces*, 1st ed., Springer International Publishing, Cham, Switzerland **2018**.
[14] V. N. Strocov, T. Schmitt, U. Flechsig, T. Schmidt, A. Imhof, Q. Chen, J. Raabe, R. Betemps, D. Zimoch, J. Krempasky, X. Wang, M. Grioni, A. Piazzalunga, L. Patthey, *J. Synchrotron Radiat.* **2010**, *17*, 631.

[15] S. M. Walker, F. Y. Bruno, Z. Wang, A. de la Torre, S. Riccó, A. Tamai, T. K. Kim, M. Hoesch, M. Shi, M. S. Bahramy, P. D. C. King, F. Baumberger, *Adv. Mater.* **2015**, *27*, 3894.
[16] V. N. Strocov, A. Chikina, M. Caputo, M.-A. Husanu, F. Bisti, D. Bracher, T. Schmitt, F. Miletto Granozio, C. A. F. Vaz, F. Lechermann, *Phys. Rev. Materials* **2019**, *3*, 106001.
[17] L. Dudy, M. Sing, P. Scheiderer, J. D. Denlinger, P. Schütz, J. Gabel, M. Buchwald, C. Schlueter, T.-L. Lee, R. Claessen, *Adv. Mater.* **2016**, *28*, 7443.
[18] B. Cheng, X. Liu, J. Hu, *Micro and Nanostructures* **2022**, *167*, 107183.
[19] P. Catrou, S. Tricot, G. Delhaye, J.-C. Le Breton, P. Turban, B. Lépine, P. Schieffer, *Phys. Rev. B* **2018**, *98*, 115402.
[20] R. Arras, J. Gosteau, S. Tricot, P. Schieffer, *Phys. Rev. B* **2020**, *102*, 205307.
[21] Q. Fu, T. Wagner, *J. Phys. Chem. B* **2005**, *109*, 11697.
[22] M. H. Hamed, R. A. Hinz, P. Lömker, M. Wilhelm, A. Gloskovskii, P. Bencok, C. Schmitz-Antoniak, H. Elnaggar, C. M. Schneider, M. Müller, *ACS Appl. Mater. Interfaces* **2019**, *11*, 7576.
[23] M. H. Hamed, D. N. Mueller, M. Müller, *J. Mater. Chem. C* **2020**, *8*, 1335.
[24] V. N. Strocov, X. Wang, M. Shi, M. Kobayashi, J. Krempasky, C. Hess, T. Schmitt, L. Patthey, *J. Synchrotron Radiat.* **2014**, *21*, 32.
[25] J. Braun, J. Minár, S. Mankovsky, V. N. Strocov, N. B. Brookes, L. Plucinski, C. M. Schneider, C. S. Fadley, H. Ebert, *Phys. Rev. B* **2013**, *88*, 205409.
[26] A. Ohtomo, D. A. Muller, J. L. Grazul, H. Y. Hwang, *Nature* **2002**, *419*, 378.
[27] P. Zhang, P. Richard, T. Qian, Y.-M. Xu, X. Dai, H. Ding, *Rev. Sci. Instrum.* **2011**, *82*, 043712.
[28] V. Strocov, ARPESView, **2022**, https://www.psi.ch/en/sls/adress/manuals.
[29] C. Elsässer, N. Takeuchi, K. M. Ho, C. T. Chan, P. Braun, M. Fähnle, *J. Phys.: Condensed Matter* **1990**, *2*, 4371.
[30] F. Lechermann, F. Welsch, C. Elsässer, C. Ederer, M. Fähnle, J. M. Sanchez, B. Meyer, *Phys. Rev. B* **2002**, *65*, 132104.
[31] D. Vogel, P. Krüger, J. Pollmann, *Phys. Rev. B* **1996**, *54*, 5495.
[32] W. Körner, C. Elsässer, *Phys. Rev. B* **2010**, *81*, 085324.
[33] J. P. Perdew, A. Zunger, *Phys. Rev. B* **1981**, *23*, 5048.
[34] F. Lechermann, W. Körner, D. F. Urban, C. Elsässer, *Phys. Rev. B* **2019**, *100*, 115125.